Scanning internal photoemission microscopy for the identification of hot carrier transport mechanisms

D. Differt,[1] W. Pfeiffer,[1,a)] and D. Diesing[2]

[1]*Fakultät für Physik, Universität Bielefeld, Universitätsstraße 25, 33615 Bielefeld, Germany*
[2]*Fakultät für Chemie, Universität Duisburg-Essen, Universitätsstraße 5, 45117 Essen, Germany*

Linear and nonlinear internal photoemission in a thin-film metal-insulator-metal heterosystem, i.e., a Ta-TaO$_x$-Ag junction, together with surface reflectivity are mapped with a lateral resolution of better than 5 μm. The spatial correlation of the different signals and time-resolved internal photoemission spectroscopy reveal excitation mechanisms and ballistic hot carrier injection. The internal photoemission yield variation with Ag layer thickness is quantitatively explained by above-barrier injection. The hot-spot-like behavior of the two-photon induced internal photoemission observed for short pulse excitation is attributed to local field enhancements because of Ag-film thickness reduction and plasmonic effects at structural defects. © *2012 American Institute of Physics*. [http://dx.doi.org/10.1063/1.4752734]

Hot carrier transport and relaxation are important for various applications such as in photovoltaic cells,[1] photo detectors,[2] light emitting devices,[3] chemocurrent sensors,[4] or cold-cathode electron emitters.[5] The carrier excess energy finds applications in energy conversion and electronic switching.[6] Depending on the particular application, efficient excited carrier transport that is limited by ultrafast scattering is either desired or undesired. The scattering of excited electrons in metals has been intensely studied using time- and energy-resolved spectroscopies.[7–9] For homogeneous systems it is described by a Fermi liquid behavior[10] and ranges from few femtoseconds for about one eV excess energy above the Fermi level to several 100 fs for thermal energies. In the ballistic transport regime this corresponds to length scales of 1 nm to 100 nm, assuming a Fermi velocity of 10^6 m s^{-1}. Hence, the impact of scattering on carrier transport can be studied in heterostructures with variable thicknesses of metal layers in the mentioned range. Time-resolved nonlinear spectroscopy such as two-photon photoemission directly provides information about scattering and transport processes of excited carriers,[9] whereas spatially resolved techniques such as ballistic electron emission microscopy[11] need a detailed modeling to obtain information about scattering and relaxation processes. Two-photon photoemission reveals state selective relaxation and transport dynamics for excited charge carriers.[9] Carrier dynamics at buried layers or interfaces can be studied by two-photon internal photoemission in heterostructures.[12,13] Similar to scanning photoemission microscopy[14] the latter method offers the possibility for a spatially resolved investigation of hot carrier transport mechanisms as demonstrated here. In this work we present spatially resolved internal photoemission (IPE) microscopy of carrier transport, relaxation, and over-the-barrier carrier injection processes in a Ta-TaO$_x$-Ag metal-insulator-metal junction (MIM). The correlation of local one-photon or two-photon internal photoemission currents and local reflectivity provides information on hot carrier transport mechanisms. Lateral inhomogenities such as thickness variations of the top electrode, the variation of the transport efficiency through the oxide, and the nonlinear photon-electron interaction in the top layer are identified.

Figure 1(a) shows the structure of the MIM device. Only the electron excitation and transport channels are indicated since hole transport is negligible. Because of the internal field E_b and the asymmetric excitation the photocurrent is dominated by electrons originating in the Ag film and injected into the Ta electrode.[15,16] The spatial resolution is achieved by a spatially confined excitation using a reflective microscope objective (Ealing x25, NA = 0.4, measured 5 μm e^{-2} focus diameter) (Fig. 1(b)). Either continuous wave illumination at 402 nm ($\approx$3.1 eV, laser diode) or pulsed illumination at 795 nm ($\approx$1.55 eV, Ti:Sapphire laser, 80 MHz repetition rate, 30 fs) is used. For measuring the surface reflectance a photodiode collects the backscattered light. The tantalum electrode is directly connected to a lock-in amplifier which provides a low noise measurement of the laser-induced current. As the sample is mounted on a *xy*-translation stage, both surface reflectivity and photo-current can be mapped down to the minimal translation stage step size of 100 nm. The MIM junctions are Ta-TaO$_x$-Ag junctions with a 40 nm thick Ag top electrode and a 4 nm TaO$_x$ layer as the insulator grown on a Ta layer.[16]

Figure 2 shows maps of the local current for cw (continuous wave) 400 nm excitation (Fig. 2(a)), the surface reflectivity at 402 nm (Fig. 2(b)), and the current for ultrashort pulse excitation at 800 nm (Fig. 2(c)). For excitation with 402 nm (Fig. 2(a)) a continuous signal is observed that is denoted as one-photon internal photoemission (1P-IPE) since it varies linearly with laser intensity and can be attributed to internal photoemission over the barrier as shown below (discussion of Fig. 3). The 1P-IPE signal shows lateral variations by a factor of two on a length scale of several 100 μm. In addition, small, spatially confined areas (several 10 μm diameter) appear with above and below average yield. These confined areas are either correlated or anticorrelated with localized regions of reduced surface reflectivity (Fig. 2(b)). As discussed below this behavior can be explained by the

a)Author to whom corresponding should be addressed. Electronic mail: pfeiffer@physik.uni-bielefeld.de.
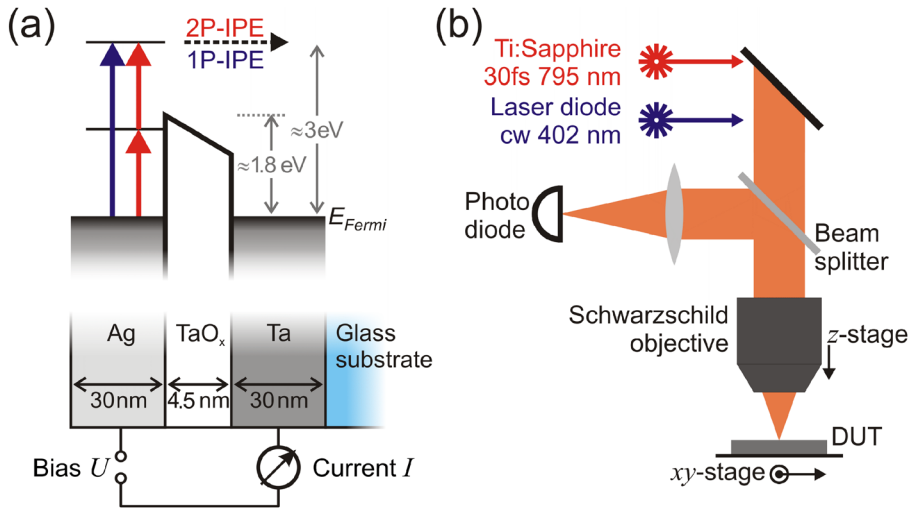
101, 111608-1

FIG. 1. Excitation scheme and experimental setup. (a) Schematic band structure of the MIM junction with one-photon (blue) and two-photon (red) excitation for 1P-IPE and 2P-IPE. (b) An aberration-corrected Schwarzschild objective focuses the light sources onto the MIM junction that is mounted as a device under test (DUT) on a *xy*-translation stage. The back-reflected light is picked up by a beam splitter and detected with a photodiode.

non-monotonous Ag film thickness dependence of the 1P-IPE yield. In contrast, the large scale 1P-IPE variations are not correlated to the surface reflectivity. Optical reflectivity calculations for the given heterostructure show that the reflectivity is determined by the silver layer thickness. For example a MIM with 20 nm thick Ag-film exhibits at 400 nm a 15%–20% reduced reflectivity as compared to a 40 nm thick film. The large scale homogeneity of the reflectivity indicates a Ag layer thickness variation of less than 10 nm. As shown below such small thickness variations of a 40 nm thick Ag film cannot account for the observed 1P-IPE variation of about 50% (compare Fig. 3). This suggests that the large scale 1P-IPE variations reflect a lateral change of carrier injection efficiency most likely determined by tunnel barrier or interface properties.

Under excitation with ultrashort laser pulses at 800 nm (30 fs duration, 5×10^9 W cm^{-2} peak intensity) the photocurrent map (Fig. 2(c)) exhibits a strikingly different behavior compared to cw 402 nm excitation (Fig. 2(a)). The photocurrent map is now completely dominated by local maxima, denoted in the following as hot-spots, and on the remaining areas the current stays below the detection limit of about 10 pA. The positions of these hot-spots are also indicated in the reflectivity map. The appearance of hot-spots is not related to laser-induced damage since the observed pattern is reproducibly obtained for successive scans, and the effect was observed on several samples at various laser fluences. Note that most of the hot-spots are related to a locally decreased reflectivity. In the case of 795 nm wavelength the highest electronic state excited in a one-photon process lies at about 0.3 eV below the upper edge of the tunnel barrier (≈ 1.8 eV), and hence no internal photoemission into the Ta layer occurs after one-photon excitation. However, the high peak intensities achieved in ultrashort pulse excitation ($\approx 5 \times 10^9$ W cm^{-2}) allow for two-photon processes leading to two-photon internal photoemission (2P-IPE). This assignment is corroborated by the nonlinear intensity dependence of the local current for one particular hot-spot shown in Fig. 2(d) and the nonlinear two-pulse correlation measurement shown in Fig. 4(c). The power law exponent of 2.4 indicates a mixture of two- and three-photon-induced processes with a dominating two-photon contribution. Both 1P-IPE and 2P-IPE rely on the transport of photoexcited carriers. How-

ever both signals behave completely differently and reveal complementary information on the excitation and transport of hot carriers as exemplified in the following.

First, the 1P-IPE yield as a function of Ag-film thickness is analyzed. Measurements and calculations show that the Ag film thickness determines the reflectivity of the MIM junction and thus critically determines the hot carrier concentration at the internal interface.[17] The 1P-IPE variation with the Ag film thickness is measured at the edge of the MIM device (Fig. 3). There the thickness of the Ag film decreases continuously over a lateral width of about 50 μm because of the shadow mask used for Ag evaporation. For positions $y < 30$ μm the bare TaO$_x$ surface is illuminated and the 1P-IPE drops to zero, whereas for $y > 90$ μm the full Ag film thickness d_{Ag} is established and an almost constant 1P-IPE yield of about 10 nA is observed. Between these points, the 1P-IPE yield doubles for an optimal film thickness of about 10 nm. The thickness dependence of the 1P-IPE signal agrees well with the 1P-IPE behavior seen in IPE microscopy (Fig. 2), i.e., a reduction of Ag film thickness can lead both to an increased and a reduced IPE yield, depending on the local film thickness. Based on the known parameters for optical properties,[18] the energy dependent mean free path of electrons, the tunnel barrier parameters,[19] and the density of states for a free electron gas, one can estimate the internal photoemission yield using a parameter-free model (dotted line in Fig. 3) that quantitatively describes the measured thickness dependence of the 1P-IPE yield (solid line in Fig. 3). The local excited electron density $n_{ex}(z)$ induced by linear absorption is calculated using the optical properties of the materials, taking into account multiple reflections in the layered structure.[16] Based on n_{ex}, the excited electron mean-free path λ for Ag $\lambda_{Ag} = 20$ nm (Ref. 20) and Ta $\lambda_{Ta} = 3$ nm as derived from excited electron lifetimes 2 eV above the Fermi energy E_F,[21] and an internal transmission coefficient η, the relative 1P-IPE yield is calculated using

$$Y_{1P-IPE}^{Ag \rightarrow Ta} = \theta \int_0^{d_{Ag}} \int_{E_F}^{E_F + \hbar\omega} \eta\, n_{ex}(z, E) \exp\left(-\frac{d_{Ag} - z}{\lambda_{Ag}}\right) dE\, dz. \quad (1)$$

The ratio θ of excited-electrons to those in the ground state depends on the incident laser power and the total absorbed
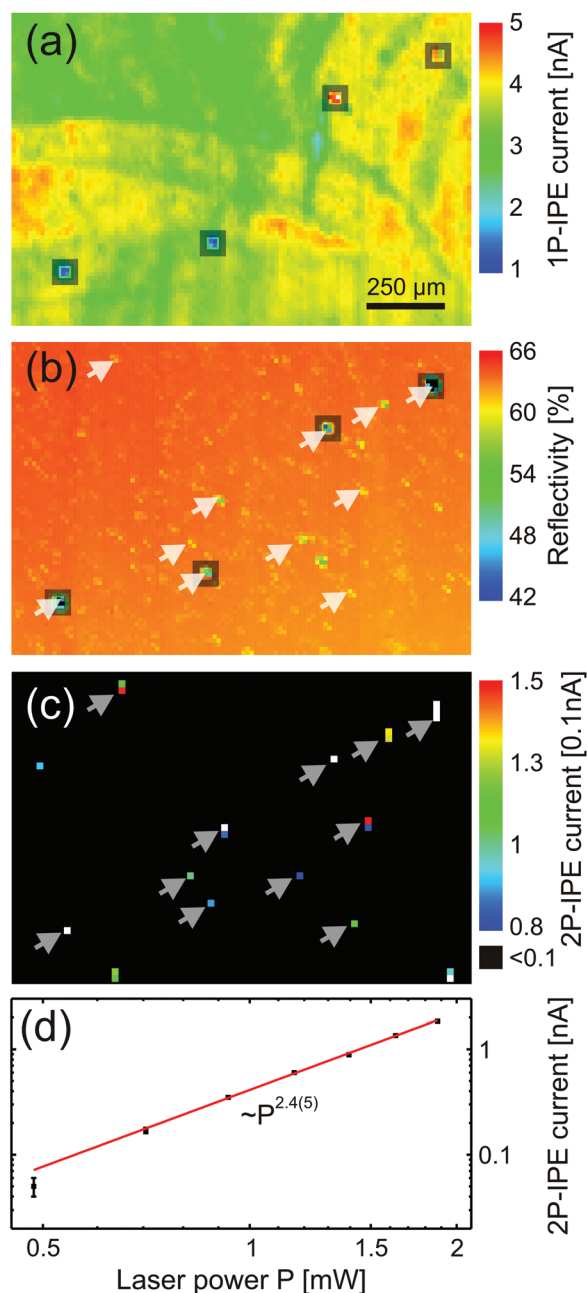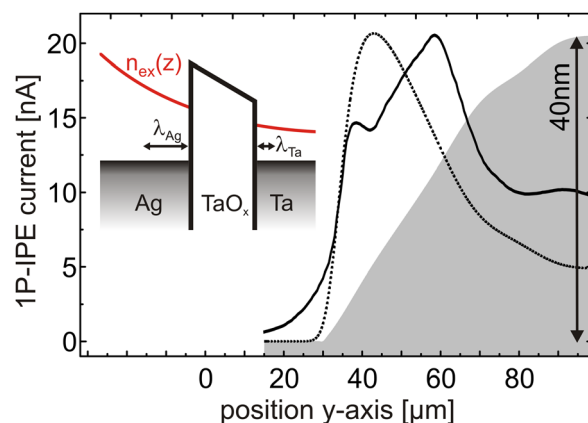
FIG. 3. 1P-IPE current variation with Ag film thickness. Measured (solid black line) and simulated (dotted black line) 1P-IPE yield variation across the edge of the Ag film for 402 nm cw illumination. The local Ag film thickness measured for an identically prepared Ag film is shown as a gray shaded height profile. The model used to derive the simulated yield is schematically represented in the inset.

FIG. 2. Scanning internal photoemission microscopy and surface reflectivity. (a) 1P-IPE map recorded with $8\,\mu m$ raster step width (cw, 402 nm, $10^3\,W\,cm^{-2}$). Gray squares indicate correlated and anti-correlated features of local 1P-IPE and reflectivity shown in part (b). (b) Reflectivity map for 402 nm radiation recorded with $15\,\mu m$ raster step width. (c) 2P-IPE map recorded with $26\,\mu m$ raster step width and pulsed laser excitation (30 fs, 795 nm, $3.1 \times 10^7\,W\,cm^{-2}$ peak intensity). Gray arrows indicate 2P-IPE hot-spots that are correlated with locally decreased surface reflectivity. For comparison these arrows are also shown in part (b). (d) Laser power dependence of the 2P-IPE yield for one particular hot-spot including power law fit to the data (red line).

fluence. η is assumed to be unity and thus independent of the excited electron energy. The net current is calculated using Eq. (1) and the corresponding expression for the counter Ta back-electrode calculating the reverse IPE from the Ta into the Ag-layer. For a thin Ag layer the absorption in the top electrode is too small to generate a strong net internal photoemission into the Ta layer. For a layer thickness similar to the penetration depth and mean-free path λ_{Ag} the IPE yield is maximal. For a larger Ag film thickness the excited electron

distribution is removed further from the interface leading to a reduced IPE yield. Note that the model is based on ballistic hot carrier transport leading to IPE and thus the good quantitative agreement between measured yield and the parameter-free model shows that indeed hot carrier injection is responsible for the observed photon induced signals.

Having identified the transport mechanism for cw 402 nm excitation we now focus on 2P-IPE. Figure 4 shows a high resolution 2P-IPE scan of two neighboring hot-spots (Fig. 4(a)) together with the local surface reflectivity (Fig. 4(b)). The 2P-IPE map shows features with less than $1\,\mu m$ lateral size, i.e., significantly smaller than the measured focus diameter. The 2P-IPE hot-spots are always correlated with minima in the surface reflectivity (Figs. 4(a) and 4(b) and arrows in Figs. 2(b) and 2(c)). In principle there are two possible mechanisms explaining this behavior of the 2P-IPE signal: Either again a local Ag film thickness reduction leads to an increased IPE yield and the nonlinearity increases the signal contrast giving rise to the hot-spot behavior, or local structural defects enhance the coupling of incident radiation into the Ag film via an optical antenna effect, leading to local field enhancements and thus explaining the locally enhanced IPE signals. Both mechanisms could act simultaneously. A resonant antenna assisted coupling mechanism that is further enhanced by the involved multiphoton excitation could also explain the spatial features well below the optical resolution of the setup since the coupling of focused radiation fields to a localized plasmonic mode depends critically on the focus position.

Further evidence about the excitation and transport mechanism is deduced from interferometric time-resolved, two-pulse correlation measurements of the photoinduced internal photoemission current (Fig. 4(c)). The IPE induced by two ultrashort laser pulses produced in a phase stabilized Mach-Zehnder interferometer[13] is recorded as a function of the delay τ between the two pulses. For τ smaller than about twice the pulse duration the signal exhibits interference fringes caused by either constructive or destructive interference of the excitation pulses. For comparison, the second order pulse autocorrelation recorded using second harmonic generation (SHG) in a $20\,\mu m$ thick beta barium borate nonlinear optical crystal is
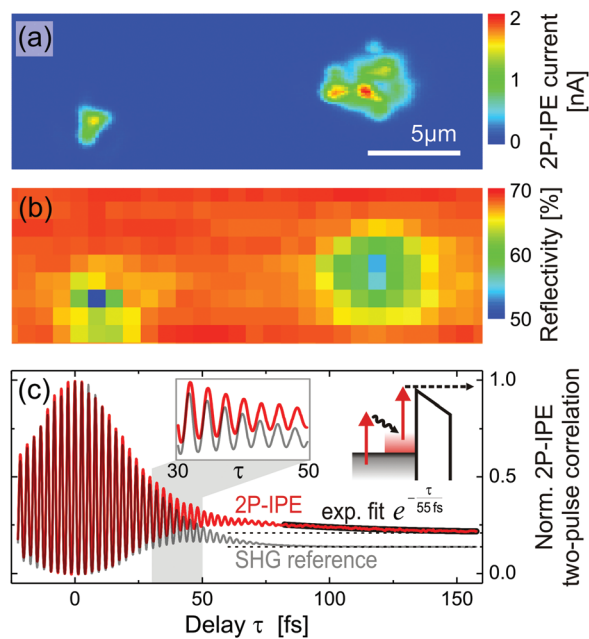
FIG. 4. Two-photon internal photoemission current mapping (a) high-resolution map of the local two-photon internal photoemission current (2P-IPE) induced by 30 fs laser pulses at 800 nm and a fluence per pulse of 1.2×10^{-10} J cm^{-2} recorded with 100 nm raster step width (9.1×10^{7} W cm^{-2} peak intensity). (b) Reflectivity pattern for 400 nm illumination recorded for the same sample area with a raster step width of 900 nm. (c) Normalized 2P-IPE two-pulse correlation signal (red) for excitation of the left hot-spot shown in part (a). For comparison the simultaneously measured second order nonlinear autocorrelation of the used laser pulses is shown (gray). The fitted exponential decay of the 2P-IPE signal for delay $\tau > 80$ fs (black) corresponds to a lifetime of 55(10) fs. The horizontal dashed lines indicate the signal levels for infinite delay τ. The mechanism responsible for this lifetime effect is schematically depicted in the upper right corner.

shown (Fig. 4(c) gray line). For a larger delay the IPE yield decreases exponentially and the ratio $Y_{2P-IPE}(\tau = \infty) : Y_{2P-IPE}(\tau = 0)$ is about 1:8 as expected for a second order nonlinear process, confirming the identification as a two-photon induced signal. The exponential decay of the $Y_{2P-IPE}(\tau)$ reflects an intermediate state lifetime of about 50 fs. In silver this is roughly the lifetime for electronic states 1 eV above the Fermi level.[9] Hence, states in this energy range are the dominating intermediate states. These states are populated by the first excitation pulse either directly or in a process including an additional scattering event as depicted schematically in Fig. 4(c). From this we conclude that the dominating hot carrier injection channel in the given metal-insulator-metal heterostructure appears about 2.5 eV above the Fermi level, and we can indeed attribute the two-photon induced signal also to internal photoemission above the tunnel barrier.

The interference fringes in the 2P-IPE two-pulse correlation signal extend to a slightly longer delay compared to the SHG reference signal and exhibit a phase shift (inset in Fig. 4(c)). This indicates that a resonance slightly detuned from the excitation wavelength is involved in the excitation process as was observed in interferometrically resolved two-photon photoemission from metal nanoparticles.[22] Interesting candidates explaining this resonant coupling are localized surface plasmon polaritons forming at the local structural defects that could act as local optical nanoantennas. This enhancement mechanis has recently been used to improve the photo-

response of MIM devices.[23] This would also support the explanation of the complex features observed in the 2P-IPE map (Fig. 4(a)) that exhibit strong signal variations at length scales well below the focus diameter.

Summarizing, we have shown that the 1P-IPE yield depends critically on the top electrode thickness and gives insight into hot carrier excitation and injection mechanisms. Furthermore time-resolved 2P-IPE reveals the excited carrier relaxation time and shows that collective plasmonic excitations enhance the local excitation via an antenna resonance and thus lead to a hot-spot like IPE yield pattern demonstrating the potential of combined 1P-IPE, 2P-IPE, and reflectivity microscopy for investigating carrier dynamics in layered heterostructures. Light induced ballistic transport is of particular interest if the relevant system dimensions are in the same range as the mean free path. The results presented here demonstrate that MIM junctions in combination with optical nanoantennas and illumination with fs light pulses offer a route towards realization of nanoscale ultrafast electron injector devices that are interesting for nanophotonic applications.

[1]C. J. Brabec, N. S. Sariciftci, and J. C. Hummelen, Adv. Funct. Mater. **11**, 15 (2001).
[2]F. Wang and N. A. Melosh, Nano Lett. **11**, 5426 (2011).
[3]M. A. Baldo, M. E. Thompson, and S. R. Forrest, Nature (London) **403**, 750 (2000).
[4]D. Diesing, G. Kritzler, M. Stermann, D. Nolting, and A. Otto, J. Solid State Electrochem. **7**, 389 (2003).
[5]L. B. Thomsen, G. Nielsen, S. B. Vendebo, M. Johansson, O. Hansen, and I. Chorkendorff, J. Vac. Sci. Technol. B. **27**, 562 (2009).
[6]K. M. Kim, B. J. Choi, D. S. Jeong, and C. S. Hwang, Appl. Phys. Lett. **89**, 162912 (2006).
[7]C. A. Schmuttenmaer, M. Aeschlimann, H. E. Elsayedali, R. J. D. Miller, D. A. Mantell, J. Cao, and Y. Gao, Phys. Rev. B **50**, 8957 (1994).
[8]T. Hertel, E. Knoesel, M. Wolf, and G. Ertl, Phys. Rev. Lett. **76**, 535 (1996).
[9]M. Aeschlimann, M. Bauer, S. Pawlik, R. Knorren, G. Bouzerar, and K. H. Bennemann, Appl. Phys. A **71**, 485 (2000).
[10]J. J. Quinn, Phys. Rev. **126**, 1453 (1962).
[11]W. J. Kaiser and L. D. Bell, Phys. Rev. Lett. **60**, 1406 (1988).
[12]D. Diesing, M. Merschdorf, A. Thon, and W. Pfeiffer, Appl. Phys. B. **78**, 443 (2004).
[13]A. Thon, M. Merschdorf, W. Pfeiffer, T. Klamroth, P. Saalfrank, and D. Diesing, Appl. Phys. A **78**, 189 (2004).
[14]V. Schweikhard, A. Grubisic, T. A. Baker, and D. J. Nesbitt, J. Phys. Chem. C **115**, 83 (2011).
[15]P. H. P. Koller, H. J. M. Swagten, W. J. M. de Jonge, H. Boeve, and R. Coehorn, Appl. Phys. Lett. **84**, 4929 (2004).
[16]P. Thissen, B. Schindler, D. Diesing, and E. Hasselbrink, New. J. Phys. **12**, 113014 (2010).
[17]D. A. Kovacs, J. Winter, S. Meyer, A. Wucher, and D. Diesing, Phys. Rev. B **76**, 235408 (2007).
[18]E. D. Palik, *Handbook of Optical Constants of Solids*, (Academic, New York, 1997).
[19]K. Stella, D. A. Kovacs, D. Diesing, W. Brezna, and J. Smoliner, J. Electrochem. Soc. **158**, P65 (2011).
[20]C. J. Tung, J. C. Ashley, and R. H. Ritchie, Surf. Sci. **81**, 427 (1979).
[21]M. Aeschlimann, S. Pawlik, and M. Bauer, Ber. Bunsen-Ges. Phys. Chem. **99**, 1504 (1995).
[22]M. Merschdorf, C. Kennerknecht, and W. Pfeiffer, Phys. Rev. B **70**, 193401 (2004).
[23]J. A. Bean, A. Weeks, and G. D. Boreman, IEEE J. Quantum Electron. **47**, 126 (2011).